JOURNAL OF SYNCHROTRON RADIATION
ISSN 1600-5775

Live small-animal X-ray lung velocimetry and lung micro-tomography at the Australian Synchrotron Imaging and Medical Beamline

Rhiannon P. Murrie,[a]* Kaye S. Morgan,[a] Anton Maksimenko,[b] Andreas Fouras,[c] David M. Paganin,[a] Chris Hall,[b] Karen K. W. Siu,[a] David W. Parsons[f,d,e] and Martin Donnelley[f,d,e]

[a]School of Physics and Astronomy, Monash University, Clayton, VIC 3800, Australia, [b]Imaging and Medical Beamline, Australian Synchrotron, Clayton, VIC 3800, Australia, [c]Division of Biological Engineering, Monash University, Clayton, VIC 3800, Australia, [d]Robinson Research Institute, University of Adelaide, SA 5001, Australia, [e]School of Paediatrics and Reproductive Health, University of Adelaide, SA 5001, Australia, and [f]Respiratory and Sleep Medicine, Women's and Children's Hospital, 72 King William Road, North Adelaide, SA 5006, Australia.
*Correspondence e-mail: rhiannon.murrie@monash.edu

Received 15 December 2014
Accepted 24 March 2015

Edited by J. F. van der Veen

Keywords: lung; X-ray; velocimetry; microtomography; phase contrast.

Supporting information: this article has supporting information at journals.iucr.org/s

The high flux and coherence produced at long synchrotron beamlines makes them well suited to performing phase-contrast X-ray imaging of the airways and lungs of live small animals. Here, findings of the first live-animal imaging on the Imaging and Medical Beamline (IMBL) at the Australian Synchrotron are reported, demonstrating the feasibility of performing dynamic lung motion measurement and high-resolution micro-tomography. Live anaesthetized mice were imaged using 30 keV monochromatic X-rays at a range of sample-to-detector propagation distances. A frame rate of 100 frames s^{-1} allowed lung motion to be determined using X-ray velocimetry. A separate group of humanely killed mice and rats were imaged by computed tomography at high resolution. Images were reconstructed and rendered to demonstrate the capacity for detailed, user-directed display of relevant respiratory anatomy. The ability to perform X-ray velocimetry on live mice at the IMBL was successfully demonstrated. High-quality renderings of the head and lungs visualized both large structures and fine details of the nasal and respiratory anatomy. The effect of sample-to-detector propagation distance on contrast and resolution was also investigated, demonstrating that soft tissue contrast increases, and resolution decreases, with increasing propagation distance. This new capability to perform live-animal imaging and high-resolution micro-tomography at the IMBL enhances the capability for investigation of respiratory diseases and the acceleration of treatment development in Australia.

1. Introduction and objectives

The Australian Synchrotron (AS) Imaging and Medical beamline (IMBL) achieved first light in the near-storage-ring hutch in 2008 (Stevenson *et al.*, 2010). Near-beam surgical and experimental facilities, the IMBL satellite building and a beam transfer tunnel have subsequently been completed, and a new superconducting multi-pole wiggler (SCMPW) was installed in February 2013. Along with radiotherapy research, the IMBL is primarily designed for performing propagation-based phase-contrast X-ray imaging (PB-PCXI) due to its high coherence and intensity, as well as its large source-to-sample distance (greater than 137 m in the satellite building hutch). The beamline setup produces an X-ray beam of up to 400 mm × 40 mm (W × H) at the sample position, making the imaging of larger animals, such as ferrets, sheep, pigs and potentially humans, possible in the future.

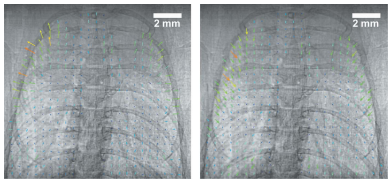

The first monochromatic X-ray tomography experiments conducted at the IMBL have been reported by Stevenson *et al.* (2012). Their study primarily characterized the beamline, and utilized a phantom comprising nylon line, aluminium wire and finer copper wire twisted together, imaged at four different X-ray energies. The feasibility of performing phase-contrast X-ray lung imaging on the IMBL has been examined by Murrie *et al.* (2014), who performed experiments using a 1.4 T multi-pole wiggler (MPW) (Hausermann *et al.*, 2010) prior to installation of the SCMPW, and demonstrated that PB-PCXI of lung phantoms at 30 keV produced high-contrast images. Their results suggested that small-animal lung imaging is feasible at the IMBL, despite the required longer than desired exposure times necessary for the 1.4 T MPW. They also suggested that feasibility would increase upon installation of the SCMPW due to the increase in available flux and corresponding decrease in required exposure time to achieve a reasonable signal-to-noise ratio (SNR).

One of our primary goals is to understand and seek a long-lasting treatment for the early fatal airway disease caused by cystic fibrosis (CF). CF lung disease is produced by a shallow dehydrated airway surface liquid (ASL), which results in impaired mucociliary transit (MCT). This produces structural and functional changes to the large airways, ultimately allowing bacterial infection and inflammation to destroy the lung. Although modern clinical imaging modalities such as computed tomography (CT), magnetic resonance imaging (MRI) and ultrasound can produce three-dimensional or four-dimensional data, they lack the spatial and temporal resolution to dynamically image the lungs, particularly in small animals such as mice and rats (Dubsky *et al.*, 2012). We have therefore developed new synchrotron-based X-ray imaging methods at the SPring-8 synchrotron in Japan to directly measure ASL depth and MCT behaviour in mouse lung conducting airways and nasal airways, *i.e.* the site of the CFTR gene defect in CF mice (Grubb & Boucher, 1999), and to detect changes in lung structure (Donnelley *et al.*, 2014; Morgan *et al.*, 2013; Parsons *et al.*, 2008). In the future we plan to use the IMBL for imaging the effects of genetic and pharmaceutical treatments in larger CF animal models such as CF ferrets (Sun *et al.*, 2010).

The aim of this pilot experiment was to determine the current capabilities of the IMBL for performing live small-animal *in vivo* X-ray velocimetry (XV) and *post mortem* high-resolution small-animal micro-tomography, with a view to performing these techniques in future biomedical experiments. XV is a technique used to study the motion of complex dynamic biological tissues, such as the flow of air through the lungs and airways (Dubsky *et al.*, 2012; Fouras *et al.*, 2012) or blood through the circulatory system (Irvine *et al.*, 2008; Jamison *et al.*, 2011). X-ray phase-contrast imaging of the many alveoli of the lungs produces a characteristic speckle pattern (Kitchen *et al.*, 2004), and it is by 'tracking' the motion of this speckle pattern over successive images separated by a known (and short) time frame that the motion of the lungs can be determined.

In this study we performed the first live-animal imaging on the IMBL, demonstrating the current capabilities of the IMBL to image a live anaesthetized mouse and study the lung motion *via* XV. We also performed micro-tomography of the lungs and nasal airways of rats and mice *post mortem*, revealing the tiny airway structures in high resolution. We present here examples of dynamic lung motion tracking, CT slice reconstruction images and CT volume renderings of relevant respiratory anatomy that can be produced at the IMBL.

2. Methods

The wiggler-based Imaging and Medical Beamline at the Australian Synchrotron was used for all imaging experiments. The data were collected over two beam-time allocations under animal ethics approvals from the Women's and Children's Health Network (AE891-09-2013) and Australian Synchrotron (AS-2012-005) Animal Ethics Committees. The synchrotron storage ring operated at 3 GeV and a ring current of 200 mA for both experiments. The RMS electron beam size in the straight sections was 320 µm × 16 µm (Stevenson *et al.*, 2012), corresponding to Gaussian FWHM of 754 µm × 38 µm in the horizontal and vertical directions, respectively. The X-ray beam supplied to the IMBL was produced by the recently installed SCMPW, consisting of 30 periods in total, with a period length of 5.2 cm. It is capable of achieving a maximum field strength of 4.2 T, but this experiment utilized a 3.0 T field strength. A dual silicon Laue crystal monochromator was used to select the required energy of 30 keV. The source-to-monochromator distance was 16.15 m. All imaging was performed in the satellite building experimental hutch 3B, at a distance of ∼136 m from the storage ring (Hausermann *et al.*, 2010) using an established setup, shown by Murrie *et al.* (2014).

2.1. Animal preparation

2.1.1. X-ray velocimetry. One mouse (male C57Bl/6N, weight 20 g) was anaesthetized with 10 µl g^{-1} body weight of medetomidine (0.1 mg ml^{-1}; Orion Corporation, Finland) and ketamine (7.6 mg ml^{-1}; Parnell Laboratories, Australia) mixture, delivered by intraperitoneal (i.p.) injection, and secured in a custom three-dimensional printed capsule using micropore tape and a dental-floss loop around the incisors. Before and during imaging the mouse respired naturally, and after imaging the mouse was humanely killed by anaesthetic overdose.

2.1.2. Micro-tomography. Mice (n = 4, male Swiss, weight ∼18–20 g) and rats (n = 3, Wistar) were provided freshly killed (CO_2 asphyxiation) from the Monash Animal Research Platform. Mice were suspended in 50 ml Falcon tubes by their incisors using dental floss to hold them upright. Standard laboratory agar (Sigma A1296, 2% in distilled water) was poured around the animals at ∼313 K and allowed to cool and solidify in a 277 K fridge, to ensure that motion blur was minimized during image acquisition. Mice were allowed to

warm to room temperature prior to imaging and the dental floss was removed from the incisors. The same protocol was used for rats, except that a larger plastic container was used as the containment vessel.

2.2. Image acquisition

Projection images were captured using the 'Ruby' beam monitor (Hall *et al.*, 2013) set up with a 25 µm terbium-doped gadolinium oxysulphide scintillator and an incorporated sCMOS detector (pco.edge; PCO Imaging, Michigan, USA) coupled *via* a Nikon 105 mm Macro zoom lens (Nikon). The incident beam was limited to the field of view using slits at the front of the imaging hutch to minimize the radiation dose and the effects of incoherent scatter.

2.2.1. X-ray velocimetry. *In vivo* images of the lungs in motion were acquired whilst the mouse was free-breathing (*i.e.* non-ventilated). To limit motion blur, the images were acquired with an exposure time of 10 ms over 10 s imaging periods, typically allowing the capture of at least ten breaths in 1000 images. A sample-to-detector propagation distance of 4.7 m was utilized to enhance the visibility of lung speckle. With the IMBL monochromator tuned to 30 keV and with a 0.2 keV bandpass, the X-ray beam flux into the experiment enclosure 3B was 3.3×10^8 photons mm^{-2} s^{-1}. This gives an air Kerma rate of 24 mGy s^{-1}. Exposures were measured with a calibrated and corrected free-air ionization chamber and verified against calculation.

2.2.2. Micro-tomography. For the mouse CT imaging an effective pixel size of 10.6 µm × 10.6 µm and a field of view of 27.1 mm × 22.9 mm (2560 × 2160 pixels) was used, and for the rat CT imaging a pixel size of 12.9 µm × 12.9 µm and field of view of 33 mm × 27.9 mm was used. In their study, Murrie *et al.* (2014) calculated that experiments imaging whole mouse lungs should utilize a sample-to-detector distance of between 1 and 4 m, with these distance ranges supported by similar studies in real lungs by Kitchen *et al.* (2004, 2008) and Lewis *et al.* (2005). They also suggest that sample-to-detector distances greater than 3 m may be negatively affected by photon scattering in air. For this reason we tested sample-to-detector distances of 0.215 m, 1.0 m, 2.0 m and 3 m. Each micro-tomography scan was set to acquire 1800 projections over 180° (*i.e.* 0.1° per image). One set of 30 flat-field and 30 dark-current images was also acquired at the beginning of each scan. Exposure lengths of 500 ms were used to produce a high SNR without movement blur, with the motors running continuously at 555 ms per 0.1°, resulting in a total acquisition time of 16.7 min. For each animal separate scans of the nasal and lung regions were performed at the selected propagation distances. In one rat a series of six overlapping scans 12 mm apart were performed to image the entire upper half (*i.e.* nose to abdomen) of the animal.

2.3. Post-experimental analyses

2.3.1. X-ray velocimetry. Given the short exposure times and the need to filter the beam to reduce the heat load on the monochromator, which resulted in a reduction to the maximum possible flux, signal averaging was required to increase the SNR of the live mouse images. This was achieved by binning the 1000 images into 14 bins, based on the image location in the phase of the breathing cycle. The position in the breath cycle was determined based on the intensity fluctuations generated as the lungs filled and emptied of air, measured within a sample region of the lungs. The images in each bin were then averaged in order to obtain the highest possible SNR. Thus, the 1000 individual raw images of >10 breaths were reduced to 14 high-SNR frames showing one breath cycle. Flat-dark correction was not applied to these images as investigation has shown better vector reconstruction without a flat-field correction. Visibility of the lung speckle was calculated as

$$\frac{I_{\mu+2\sigma} - I_{\mu-2\sigma}}{I_{\mu+2\sigma} + I_{\mu-2\sigma}} \times 100\%, \quad (1)$$

where I represents the intensity value of the image, μ the mean intensity and σ the standard deviation. A 5 pixel median filter and a 20–150 pixel bandpass frequency filter were applied to the images to reduce noise and enhance the visibility of the lung speckle relative to low-frequency background variations and high-frequency noise. A mask was also applied over the lungs so that only the lungs and airways underwent analysis. XV analysis was then performed every eight pixels, using 32 pixel × 32 pixel interrogation windows. An iterative approach was used through which initial vectors give an estimate of the displacement of the lung tissue, with further passes refining the vector lengths and directions. These vectors were then smoothed using a χ-squared method to increase the SNR of the cross-correlation peak, and the cross-correlation was re-run in order to increase vector accuracy.

2.3.2. Micro CT. In the case of phase-retrieved CT reconstructions, images were flat-field and dark-current corrected and single-image phase retrieval (Paganin *et al.*, 2002) was performed. This method requires the input of the refractive and absorptive properties, δ and β, respectively, where the X-ray refractive index, n, of the material being analysed is given by $n = 1 - \delta + i\beta$. For the samples analysed here, the δ/β ratio in the phase-retrieval filter was set to 200. The projection images were reconstructed into slices using *X-TRACT* software (version 4, http://ts-imaging.net/Services/) (Gureyev *et al.*, 2011) on the Australian Synchrotron MASSIVE computing cluster. The reconstruction algorithm utilized phase retrieval and a filtered back projection algorithm. Segmentation was performed and volumes were rendered using *Drishti* (https://github.com/AjayLimaye/drishti).

3. Results and discussion

3.1. X-ray velocimetry

Fig. 1 shows phase-contrast X-ray images of the lungs with the overlaid vectors showing the lungs in motion during (*a*) inhalation and (*b*) exhalation. The phase-contrast images have been phase-binned, and the vectors show the integrated motion vectors from the two phases of the breathing cycle. The

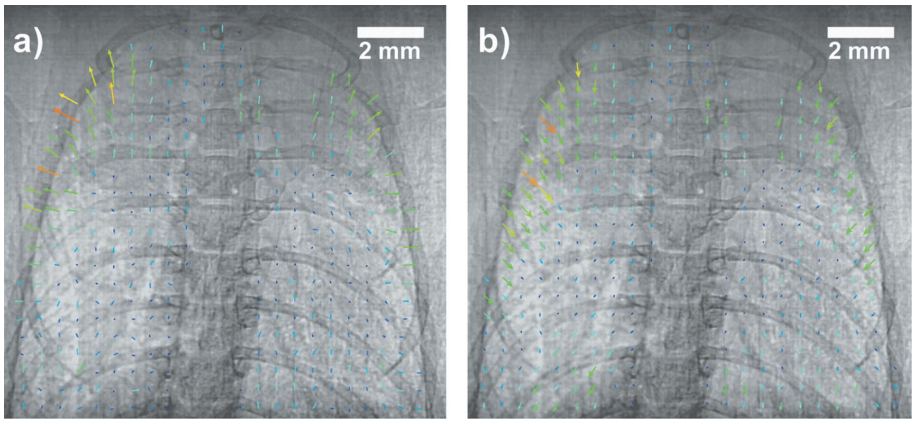

Figure 1
Live mouse lung imaged at 30 keV, R_2 = 4.7 m in hutch 3B. Exposure time was 10 ms. Overlaying XV vectors show the motion of the lungs during (*a*) inhalation and (*b*) exhalation. The full breath can be viewed in Video 1 of the supporting information.

full breath can be viewed in Video 1 of the supporting information.

The vectors accurately show the expansion and contraction of the lungs over the breath. There is some noise in the vector field where the image quality is not sufficient for the lung movement to be accurately traced. This is particularly evident towards the lower and middle regions of the lung where there are few features, such as high-contrast lung speckle, for the XV to track; in those locations there are either no vectors, vectors with a very small magnitude, or isolated vectors pointing in a direction that does not agree with the surrounding vectors. In these locations the algorithm does not have enough information pertaining to the tissue motion of that area, and has unsuccessfully tried to estimate the motion. The vectors located near the edge of the lung are of a higher quality, as the phase-contrast-enhanced-edge of the lung is easier to track.

It can be seen that the lung speckle pattern is not highly visible, with an average visibility of (11.4 ± 2.6)% in the phase-binned images, and this may be attributed to a number of factors. Firstly, the high flux produced by the SCMPW produces a high heat load on the monochromator, and thus the beam had to be filtered which limited the available flux. This meant that at an exposure time of 10 ms, which was used to limit motion blur, the images were quite noisy (10% noise), thus decreasing the SNR of the lung speckle. Although the images were binned to the breath cycle and averaged to enhance the speckle SNR, this process may result in some unintentional smoothing of the speckle if the lungs were not in exactly the same position in each bin. However, this process was necessary here to enhance the SNR to an acceptable level for XV analysis (4% noise). With further optimization of both the wiggler and beamline setup, exposure times of less than 10 ms will be achievable with a higher image SNR. This optimization is ongoing, with the flux already having been improved by approximately four times since the experiments presented here were conducted, and flux will continue to improve into the future. There are also plans to install a new pair of monochromator crystals in the future, which should further increase the available flux and thus decrease exposure times.

Additionally, due to the large horizontal source size, penumbral blur affects the speckle visibility in the horizontal direction. Furthermore, scattering of the photons in air over the large sample-to-detector propagation distance may also have contributed to decreasing the SNR, as discussed by Murrie *et al.* (2014). The accuracy of the XV analysis can be increased by improving the visibility of the speckle in the initial phase-contrast images, which will increase the SNR of the cross-correlation peaks used to calculate the displacement of the image features. Murrie *et al.* (2014) found that the optimum imaging distances for mouse lungs at the Australian Synchrotron IMBL is 3–4 m, whereas these images were taken at 4.7 m, and before the optimum distance had been determined. This highlights the scope for improvement in both image and vector quality if experiments are undertaken at optimum distances. It is important to keep in mind that on this general medical purpose beamline the large source and beam size is an asset in imaging large animals, such as sheep and pigs, and potentially humans in the future. With these applications in mind and the source and beam sizes required for such imaging, the associated penumbral blur will be a fundamental limitation to the resolution on the IMBL when imaging small samples that require a fast exposure time (such as the live imaging of small animals). However, further optimization of the beamline will allow for an increase in the available flux and will therefore allow the source size to be reduced to an extent (without limiting the faster exposure times too much), thus reducing the associated penumbral blur seen, particularly when live imaging the fine detail of the lungs in small animals. Additionally, the propagation distance can be reduced, but the spacing and visibility of the fringes will also be reduced. In addition, placing a vacuum tube or other low-scattering medium, such as helium, between the sample and detector may significantly improve the contrast of the speckle in the images.

3.2. Micro-tomography

The aim of this experiment was to produce high-quality CT images using the IMBL, so we sought to keep the animals completely still by suspending them in agarose. Using this method, projection data were successfully obtained and reconstructed for the four mice and three rats. In all reconstructions the δ/β ratio in the phase retrieval filter was set to 200. This was not the correct value for quantitative phase-retrieval of soft-tissue in air at 30 keV; however, using this value meant that the other components of the sample, such as

the bones, were not smeared out and all features could be resolved relatively clearly. The edges of the bones did not produce the bright/dark phase-contrast fringe seen at the edges of the airways, so, when phase retrieval was applied using the δ/β values for soft tissue, the edges were smoothed out beyond their correct boundaries and the bones falsely appeared to have blurry edges in the phase-retrieved reconstructed slices. For this reason, δ/β was chosen to balance the signal-enhancing phase retrieval of the soft tissue with the detrimental bone blurring. An alternative approach would be to splice together multiple reconstructions using the correct ratio of $(\delta_1 - \delta_2)/(\beta_1 - \beta_2)$ for each pair of materials (Beltran *et al.*, 2010), such as bone/soft-tissue and air/soft-tissue. Additionally, one could combine the low-frequency components of the phase-retrieved slices with the high-frequency components of edge-enhanced slices, as shown by Irvine *et al.* (2014).

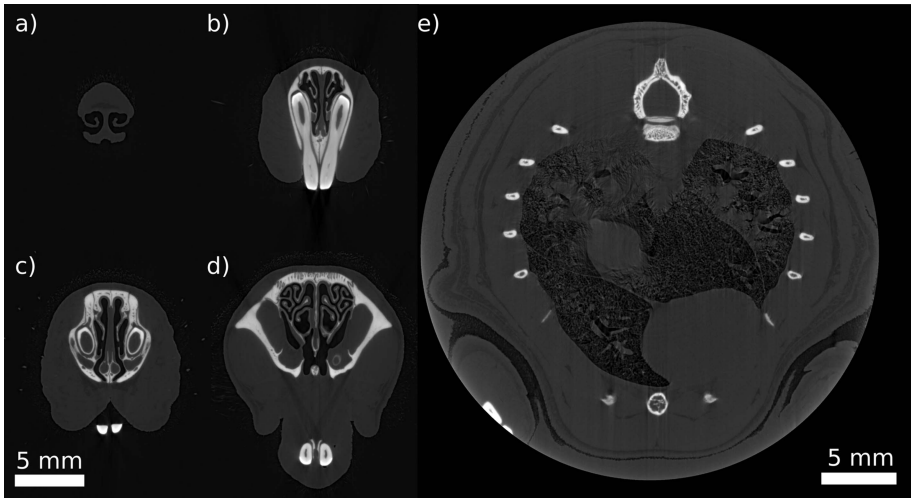

Figure 3
Example CT slices showing (*a*–*d*) the rat nose and (*e*) rat lung. Image quality could be improved in (*e*) by maintaining a fixed pressure in the lungs to prevent movement while capturing the CT sequence.

Example reconstructions of the nose of one mouse are shown in Fig. 2, with corresponding reconstructions of the rat nose shown in Fig. 3. In these slices, the harder edges of the incisor teeth are apparent, showing up as a brighter white than the bone structures. The fur and whiskers are also seen surrounding the nose and the intricate nasal passages can be traced throughout the volume. These images are of particular use in our cystic fibrosis (CF) studies as mouse models of CF only exhibit CF epithelial cell dysfunction on some surfaces of these nasal passages. A comparison between Figs. 2 and 3 also reveals the slightly smaller, rounder nature of the mouse nose compared with the rat nose, although the essential similarities of these two species of rodent are apparent. Fig. 3(*e*) shows the lungs of the rat as well as layers of fat and tissue under the skin of the rat. Part of a paw is visible in the bottom left of Fig. 3(*e*).

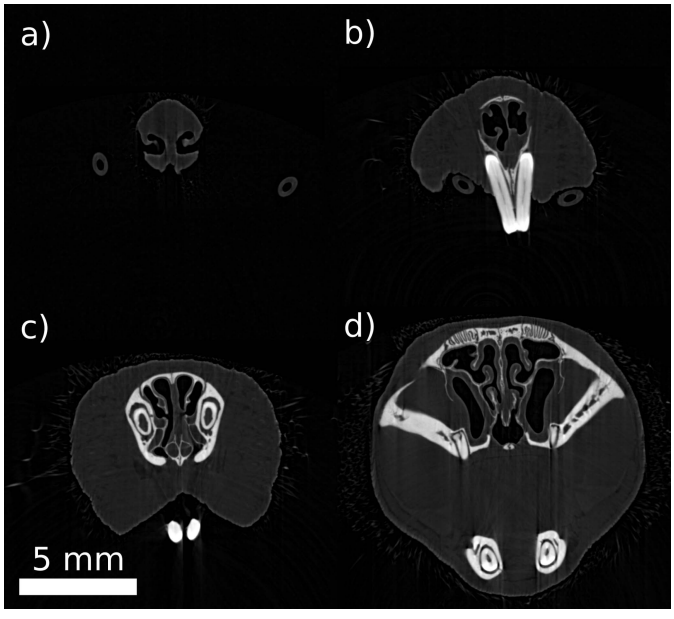

Figure 2
Example CT slices showing the mouse nose. Note that the tube structure seen on the right and the left of the nose in the top two panels is a plastic tube that is supporting the incisors and these features are not a part of the biology.

A rendering of the rat head is shown in Fig. 4, with the agar clearly visible at the neck level. A separate rendering of the complete rat respiratory system is shown in Fig. 5 (and Video 2 of the supporting information). Fig. 6 shows the ability of the technique to visualize the detailed structure and position of the bones relative to the soft tissue. Fig. 7 shows that soft tissue differentiation is possible with phase retrieval, with the eye structures visible in Fig. 7(*a*) and hair or whisker follicles visible in Figs. 7(*b*) and 7(*c*). Figs. 7(*b*) and 7(*c*) allow the airway structure of the mice and rats to be compared.

The effect of altering the propagation distance was determined by repeating the CT acquisitions at increasing sample-to-detector distances. A comparison of the resulting reconstructed slices from the nasal region of a mouse is shown in

Figure 4
Example rendering of the rat head. Note the solidified agar in the containment vessel at the neck level. A movie of the rat head is shown in Video 2 of the supporting information.

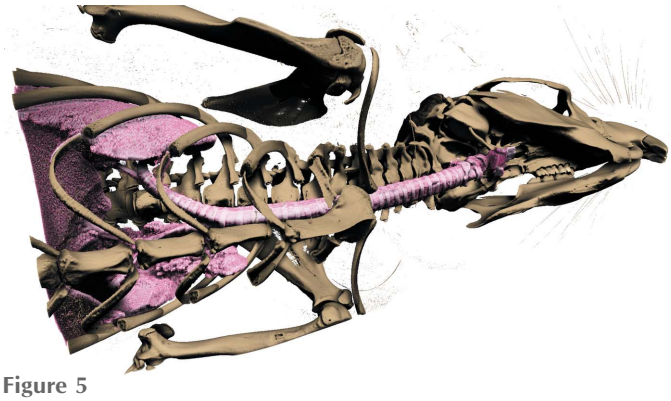

Figure 5
Rendering showing the rat skeleton and respiratory system.

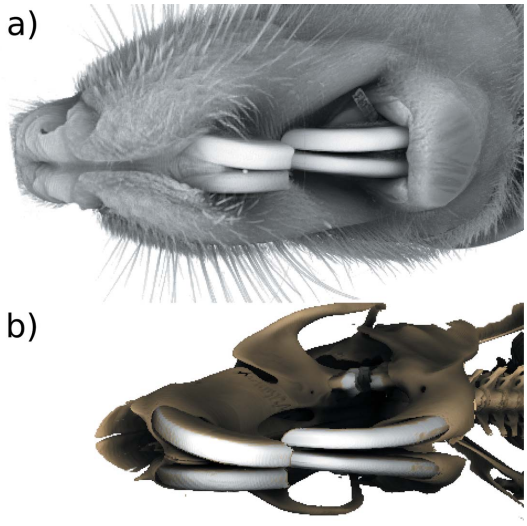

Figure 6
Rendering of the rat head, shown (*a*) with soft tissue and (*b*) with bone only, in the same position.

Fig. 8, both as a 'raw' edge-enhanced reconstruction and a phase-retrieved reconstruction. In Fig. 8(*a*), it can be seen that with 0.215 m propagation the signal-to-noise ratio is relatively low (particularly in the soft-tissue areas), with little phase contrast apparent. However, this means the edge-enhancement fringes at the airway interfaces are narrow and hence high resolution is maintained. Furthermore, the phase-retrieval process does not smear out the bones. In Fig. 8(*b*), stronger edge enhancement is apparent, and soft tissue structures connecting the lower jaw to the upper jaw are apparent with phase retrieval [Fig. 8(*f*), see red rectangle where the contrast is increased]. Moving to 2 and 3 m propagation, the detail of the fine structures begins to be blurred by the stronger phase-retrieval process (see blue circle insets), although this additional propagation increases the SNR in the soft tissue structures around the jaw (see red rectangle sections). The propagation distance should therefore be chosen according to the properties of the features of interest.

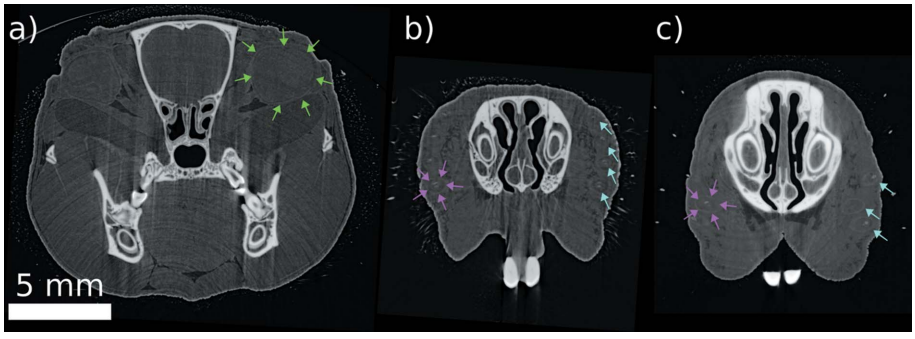

Figure 7
Soft tissue differentiation visible at 2 m propagation with phase retrieval. (*a*) Mouse eyeballs are seen caudal the nasal airways, with the boundaries indicated by the green arrows; (*b*) mouse and (*c*) rat hair or whisker follicles are seen on the tip of the nose, with the boundaries indicated by the pink arrows and positions of further follicles shown by the blue arrows.

4. Conclusion

This study details findings of the first live small-animal imaging and high-resolution lung micro-tomography on the Imaging and Medical Beamline at the Australian Synchrotron. Dynamic tracking of regional lung movement during respiration was successfully demonstrated using X-ray velocimetry, and micro-CT was able to capture the intricate airway structures of the respiratory system in high resolution and differentiate various types of soft tissue. The development of animal handling techniques, and XV and micro-tomography acquisition procedures at the IMBL, is expected to enhance and accelerate the investigation of respiratory diseases and the development of new pharmaceutical and genetic treatments.

Acknowledgements

These studies were supported by the Women's and Children's Hospital Foundation, NHMRC Australia (Project 626863) and philanthropic donors *via* the Cure4CF Foundation (http://www.cure4cf.org). This research was undertaken on the Imaging and Medical Beamline at the Australian Synchrotron, under proposal numbers AS131/IM/5211 and AS133/IM/7028. We thank Dr Andrew Stevenson, Dr Daniel Hausermann, Mr Ryan Green and Mr Simon Higgins for technical assistance on the beamline, the Monash Animal Research Platform for providing the mice and rats, and Mr Rajeev Samarage for technical assistance with the XV analysis. MD is supported by a MS McLeod Fellowship, KM by an ARC DECRA and RM by an APA. MD and DWP were supported by the Australian Synchrotron Domestic Travel Funding Program.

References

Beltran, M. A., Paganin, D. M., Uesugi, K. & Kitchen, M. J. (2010). *Opt. Express*, **18**, 6423–6436.

Donnelley, M., Morgan, K. S., Siu, K. K., Farrow, N. R., Stahr, C. S., Boucher, R. C., Fouras, A. & Parsons, D. W. (2014). *Sci. Rep.* **4**, 3689.

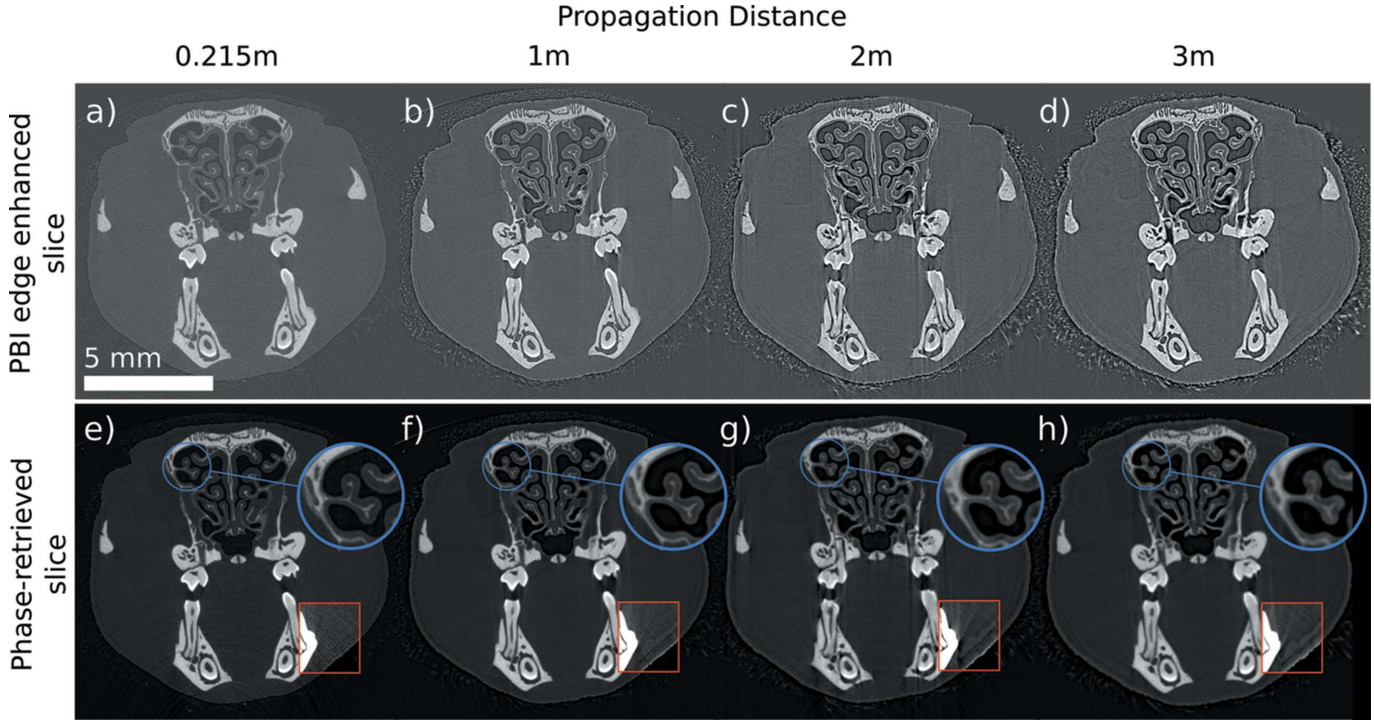

Figure 8
Panel showing the effect of propagation distance. The red boxes show enhanced contrast of soft-tissue features increasing in visibility with propagation (a different greyscale is applied in the box to display this effect). The blue circles show loss of soft-tissue resolution at longer propagation distances.

Dubsky, S., Hooper, S. B., Siu, K. K. W. & Fouras, A. (2012). *J. R. Soc. Interface*, **9**, 2213–2224.

Fouras, A., Allison, B. J., Kitchen, M. J., Dubsky, S., Nguyen, J., Hourigan, K., Siu, K. K., Lewis, R. A., Wallace, M. J. & Hooper, S. B. (2012). *Ann. Biomed. Eng.* **40**, 1160–1169.

Grubb, B. R. & Boucher, R. C. (1999). *Physiol. Rev.* **79**, S193–S214.

Gureyev, T. E., Nesterets, Y., Ternovski, D., Thompson, D., Wilkins, S. W., Stevenson, A. W., Sakellariou, A. & Taylor, J. A. (2011). *Proc. SPIE*, **8141**, 81410B.

Hall, C., Hausermann, D., Maksimenko, A., Astolfo, A., Siu, K. K. W., Pearson, J. & Stevenson, A. (2013). *J. Instrum.* **8**, C06011.

Hausermann, D., Hall, C., Maksimenko, A., Campbell, C. & Siu, K. K. W. (2010). *AIP Conf. Proc.* **1266**, 3–9.

Irvine, S., Mokso, R., Modregger, P., Wang, Z., Marone, F. & Stampanoni, M. (2014). *Opt. Express*, **22**, 27257–27269.

Irvine, S. C., Paganin, D. M., Dubsky, S., Lewis, R. A. & Fouras, A. (2008). *Appl. Phys. Lett.* **93**, 153901.

Jamison, R. A., Dubsky, S., Siu, K. K. W., Hourigan, K. & Fouras, A. (2011). *Ann. Biomed. Eng.* **39**, 1643–1653.

Kitchen, M. J., Lewis, R. A., Morgan, M. J., Wallace, M. J., Siew, M. L., Siu, K. K. W., Habib, A., Fouras, A., Yagi, N., Uesugi, K. & Hooper, S. B. (2008). *Phys. Med. Biol.* **53**, 6065–6077.

Kitchen, M. J., Paganin, D., Lewis, R. A., Yagi, N., Uesugi, K. & Mudie, S. T. (2004). *Phys. Med. Biol.* **49**, 4335–4348.

Lewis, R. A., Yagi, N., Kitchen, M. J., Morgan, M. J., Paganin, D., Siu, K. K. W., Pavlov, K., Williams, I., Uesugi, K., Wallace, M. J., Hall, C. J., Whitley, J. & Hooper, S. B. (2005). *Phys. Med. Biol.* **50**, 5031–5040.

Morgan, K. S., Donnelley, M., Paganin, D. M., Fouras, A., Yagi, N., Suzuki, Y., Takeuchi, A., Uesugi, K., Boucher, R. C., Parsons, D. W. & Siu, K. K. (2013). *PLoS One*, **8**, e55822.

Murrie, R. P., Stevenson, A. W., Morgan, K. S., Fouras, A., Paganin, D. M. & Siu, K. K. W. (2014). *J. Synchrotron Rad.* **21**, 430–445.

Paganin, D., Mayo, S. C., Gureyev, T. E., Miller, P. R. & Wilkins, S. W. (2002). *J. Microsc.* **206**, 33–40.

Parsons, D. W., Morgan, K., Donnelley, M., Fouras, A., Crosbie, J., Williams, I., Boucher, R. C., Uesugi, K., Yagi, N. & Siu, K. K. W. (2008). *J. Anat.* **213**, 217–227.

Stevenson, A. W., Hall, C. J., Mayo, S. C., Häusermann, D., Maksimenko, A., Gureyev, T. E., Nesterets, Y. I., Wilkins, S. W. & Lewis, R. A. (2012). *J. Synchrotron Rad.* **19**, 728–750.

Stevenson, A. W., Mayo, S. C., Häusermann, D., Maksimenko, A., Garrett, R. F., Hall, C. J., Wilkins, S. W., Lewis, R. A. & Myers, D. E. (2010). *J. Synchrotron Rad.* **17**, 75–80.

Sun, X., Sui, H., Fisher, J. T., Yan, Z., Liu, X., Cho, H. J., Joo, N. S., Zhang, Y., Zhou, W., Yi, Y., Kinyon, J. M., Lei-Butters, D. C., Griffin, M. A., Naumann, P., Luo, M., Ascher, J., Wang, K., Frana, T., Wine, J. J., Meyerholz, D. K. & Engelhardt, J. F. (2010). *J. Clin. Invest.* **120**, 3149–3160.